Different behaviors on the external and inner surface of hollow CdS/ V_S-MoS$_2$ heterojunctions in photoelectrocatalytic CO$_2$ reduction via SH-assisted mechanism

Chunyan Liu [a], Yejun Xiao [c], Wenrui Wan [a], Yan Wei [a], Youzhi Cao [a], Lin Hong [a], Yingqi Wang [a], Jiazang Chen [b], Qiaolan Zhang [a,*], Huanwang Jing [a,b,**]

[a] *State Key Laboratory of Applied Organic Chemistry, College of Chemistry and Chemical Engineering, Lanzhou University, 222 South Tianshui Road, Lanzhou 730000, PR China*
[b] *State Key Laboratory of Coal Conversion, Institute of Coal Chemistry, Chinese Academy of Sciences, Taiyuan 030001, PR China*
[c] *State Key Laboratory of Molecular Reaction Dynamics and Collaborative Innovation Center of Chemistry for Energy Materials (iChEM), Dalian Institute of Chemical Physics, Chinese Academy of Sciences, Dalian 116023, PR China*

ARTICLE INFO

ABSTRACT

The photoelectrocatalytic reduction of CO$_2$ to value-added chemicals is a promising methodology to address both environmental and energy issues on the earth. Herein, a hollow heterojunction of CdS/V_S-MoS$_2$ rich in S-vacancies (V_S) was designed, synthesized and applied to the photoelectrocatalytic reduction of CO$_2$. The different selectivity for products between inner and external surfaces of hollow catalysts were carefully investigated. The selectivity for C$_2$ chemicals on the inner surfaces is up to 67.0% due to the increased collision probability of the intermediates in the confined cavity. Therefore, the morphology is important to the selectivity of products in photoelectrocatalytic reduction of CO$_2$. A new mechanism of SH-assisted CO$_2$ reduction was proven by DFT calculation and the important active species such as *OCHO, *CO$_2^-$, SH (active hydrogen atom trapped by S atom) were verified obviously by the operando IR spectra on a self-installed instrument.

1. Introduction

The global CO$_2$ emission has approached to a high level of CO$_2$ concentration (420.23 ppm) in the atmosphere at 2022 according to the report of national oceanic and atmospheric administration, which is the highest datum on record of planet. In 1978, Halmann first reported the photoelectrocatalytic (PEC) reduction of CO$_2$ to chemicals using p-GaP semiconductor as catalyst [1]. This opened a new way to convert CO$_2$ and H$_2$O into valuable chemicals and would be an effective strategy to reduce the concentration of CO$_2$ in the atmosphere [2,3]. Apart from the PEC reduction, the main strategies for CO$_2$ reduction include photocatalysis (PC) [4–6] and electrocatalysis (EC) [7–9] as well. The PEC reduction of CO$_2$ combined the virtues of photocatalysis and electrocatalysis demonstrates extremely high efficiency for CO$_2$ transformation because of the enhanced separation efficiency and mobility of photogenerated carriers under the external electric field [10–12]. Up to now,

diverse semiconductor catalysts including TiO$_2$, ZnO, CdS, MoS$_2$, ZnIn$_2$S$_4$, have been investigated for PEC reduction of CO$_2$. Unfortunately, most of these single catalysts suffer from unsatisfied catalytic performance and stability owing to the low separation efficiency of photogenerated carriers and the phenomenon of photocorrosion [13, 14].

To overcome these drawbacks of single semiconductor catalysts, many methods such as morphology control, doping, fabricating defects and constructing heterojunctions were investigated [15–17]. Among them, constructing heterojunctions could be a promising way because the build-in electric field can suppress the recombination of carriers [18–20]. While the introduction of vacancy defects would serve as the active sites by means of modifying the surface structures [21–24]. Besides, the morphology design also plays an important role in their catalytic ability and selectivity with 1D, 2D and 3D catalysts [25,26]. A hexagonal CdS semiconductor has a narrow band gap of 2.4 eV and a

suitable CB (conduction band) position for photocatalysis. It was usually modified by other metals or semiconductors for constructing heterostructures to overcome the drawback of photocorrosion [27,28]. Considering a narrow band gap of 1.25 eV in MoS_2 [29,30] and similar hexagonal crystal structure in both MoS_2 and CdS, it is easy to construct heterojunctions between them.

Therefore, new heterojunctions of CdS/V_S-MoS_2 with hollow structure have been designed, synthesized and applied to PEC reduction of CO_2. On this basis, the optimal catalyst of CdS/V_S-MoS_2 could reduce CO_2 and H_2O to formate on the external surface and the polystyrene partial-covered catalyst of CdS/V_S-MoS_2-PS gives C_2 products on the inner surface. A possible SH-assisted reaction mechanism had been firstly proposed and proven by density functional theory (DFT) calculations. The C_2 products generated on the inner surface through the carbene intermediate was verfied by ^{13}C labeling experiments. The intermediates of *OCHO, *CO_2^- and SH have been confirmed by the operando IR spectra.

2. Experimental section

2.1. Sample preparation

2.1.1. Synthesis of CdS hollow nanospheres

First, SiO_2 particles with diameter of 200 nm were synthesized by the improved Stöber method [31]. To a mixed solution of 60 mL ethanol, 3 mL deionized water and 15 mL $NH_3·H_2O$, 3% TEOS ethanol solution (100 mL) was added quickly. The reaction was continued to stir for 3 h. Then, the sol-gel suspension was centrifuged, washed with deionized water and dried in vacuum at 60 °C overnight to obtain SiO_2 particles. Subsequently, 100 mg SiO_2, 6.67 mL sodium citrate (0.1 M), 5 mL $CdCl_2$ (0.1 M) and 10 mL thiourea (0.1 M) were added into 100 mL deionized water with the pH adjusting to 11 by $NH_3·H_2O$. The mixed solution was reacted at 75 °C under ultrasonic condition for 2 h to produce the yellow CdS/SiO_2 nanospheres. After etching of CdS/SiO_2 by 0.4% HF aqueous solution for about 30 min, the CdS hollow nanospheres were prepared through centrifuging, washing with deionized water and drying in vacuum at 60 °C overnight.

2.1.2. Synthesis of CdS/V_S-MoS_2 hollow nanospheres

100 mg CdS/SiO_2, 62.5 mg $Na_2MoO_4·2H_2O$ and 62.5 mg L-Cysteine were dispersed into 10 mL deionized water and stirred for 1 h. After that, the paste was moved into a microwave reactor and reacted at 200 °C for 3 h to obtain the CdS/V_S-MoS_2/SiO_2-4 spheres. Similarly, the CdS/V_S-MoS_2-4 with hollow structure was obtained by etching by 0.4% HF as above. The hollow CdS/V_S-MoS_2-x (x = 1–5) spheres with various ratios of CdS and V_S-MoS_2 were produced using different amount of $Na_2MoO_4·2H_2O$ (25, 37.5, 50, 62.5, 75 mg) and the same amount of L-Cysteine. The real molar ratios of MoS_2 and CdS were confirmed by ICP-OES analysis and shown in Table S1.

V_S-MoS_2 was prepared in the same way except for the addition of CdS/SiO_2.

2.1.3. Synthesis of CdS/MoS_2 hollow nanospheres

As comparison, CdS/MoS_2 nanospheres without S-vacancy were made by mechanically grinding CdS/V_S-MoS_2/SiO_2 nanospheres with overweight S powder in a mortar and annealing at 400 °C for 2 h under the protection of Ar gas to replenish S atoms into the materials and remove S-vacancies completely. Subsequently, it was washed with CS_2 for several times to remove the excess sulfur powder. Finally, CdS/MoS_2 hollow nanospheres were obtained in the same way as above.

2.1.4. Preparation of CdS/V_S-MoS_2-PS photocathodes

To investigate the CO_2 reduction inside the hollow nanospheres, the CdS/V_S-MoS_2 photocathode was coated with a layer of porous polystyrene. Briefly, 5 mg CdS/V_S-MoS_2 powder was dispersed in 0.5 mL nafion ethanol solution (0.5%) and then dropped onto 1 × 2 cm^2 carbon

paper with drying in vacuum at 60 °C overnight to obtain the CdS/V_S-MoS_2 photocathode. Different masses of polystyrene particles were dissolved in 20 mL of dichloromethane solution to prepare polystyrene solutions with various weight percentage (1%, 3%, 5% and 10%). Next, the CdS/V_S-MoS_2 photocathode was immersed in the polystyrene solution for 1 min, and then taken out to dry quickly. This process was repeated twice and dried in vacuum at 60 °C overnight to obtain the porous polymer-coated CdS/V_S-MoS_2-PS photocathode.

2.2. Characterization

2.2.1. General characterization

The morphology of the fabricated materials were characterized by the field emission scanning electron microscopy (FE-SEM, JSM-6701F, JEOL Inc., Japan) and transmission electron microscopy (TEM, Tecnai G2 F30, FEI, USA). X-ray powder diffraction (XRD) was recorded on X'Pert PRO diffractometer (Cu K-Alpha radiation, λ = 0.1541 nm). Raman spectra were obtained on the Zolix Finder Vista-HiR system with the excitation wavelength of 532 nm. EPR spectra were record on the EPR spectrometer (JEOL JESFA200). UV/vis absorption spectra were tested on the UV–vis spectrophotometer (UV 2600, Shimadzu). The N_2 and CO_2 adsorption/desorption isotherms were measured using Micromeritics ASAP-2020. XPS analyses were measured on a VG Scientific ESCALB210-XPS photoelectron spectrometer equipped with an Mg Kα X-ray resource. The fs-TA spectra were obtained on the femtosecond pump-probe spectrometer (ExciPro, CDP) coupled to the amplified laser system under the 400 nm pump beam. 1 mg catalyst was dispersed into 5 mL dimethyl sulphoxide (DMSO) solution for the fs-TA detection. Room temperature PL spectra were obtained on a luminescence spectrometer (Jobin Yvon Fluorolog 3-TAU, Jobin Yvon Instruments Co., Ltd., France) with the excitation wavelength of 280 nm.

2.2.2. X-ray absorption near edge structure (XANES) spectra

The X-ray absorption near edge structure (XANES) spectra were recorded on the hard X-ray Microanalysis Beamline of the Shanghai Light Source with Si (111) double crystal monochromator. The measurements of the Mo K-edge were collected in the transmission mode at room temperature. The spectra were normalized, and background subtracted on the Athena software. Fourier transformation of the k^3-weighted spectra were obtained on the k range of 0–14 Å. EXAFS fittings were performed on Artemis based on the χ(k) spectra from Athena and the χ(k) function is shown in Eq. (1). The wavelet transform EXAFS were simulated from the hama software.

$$\chi(k) = \sum_j \frac{s_0^2 N_j f_j(k) e^{-2R_j/\lambda(k)} e^{-2k^2\sigma_j^2}}{kR_j^2} \sin\left[2kR_j + \delta_j(k)\right] \tag{1}$$

where, f (k) and δ(k) are photo-electron scattering properties of the neighboring atom and λ(k) is the photo-electron mean-free-path. R is the distance to neighboring atom, N is coordination number of neighboring atom, σ^2 is Debye-Waller factor (mean-square disorder of neighbor distance).

2.2.3. Finite-element method simulations

Finite-element method (FEM) simulations were performed on COMSOL multiphysics package with "Transport of diluted species (tds)" and "Chemistry (chem)" module. Two chemical species (CO_2 and C_2) were defined as reactant and products. The "tds" module was employed to simulate the mass transfer of these two species. The diffusion constants of CO_2 and C_2 (C_2H_5OH) were set as 1.85×10^{-5} and 1.22×10^{-5} cm^2/s, respectively [32,33]. The "Chem" module defined the CO_2 reduction reaction of $CO_2 + CO_2 => C_2$. The rate constant for the formation of C_2 product was obtained from the literature [34].

2.2.4. DFT calculation

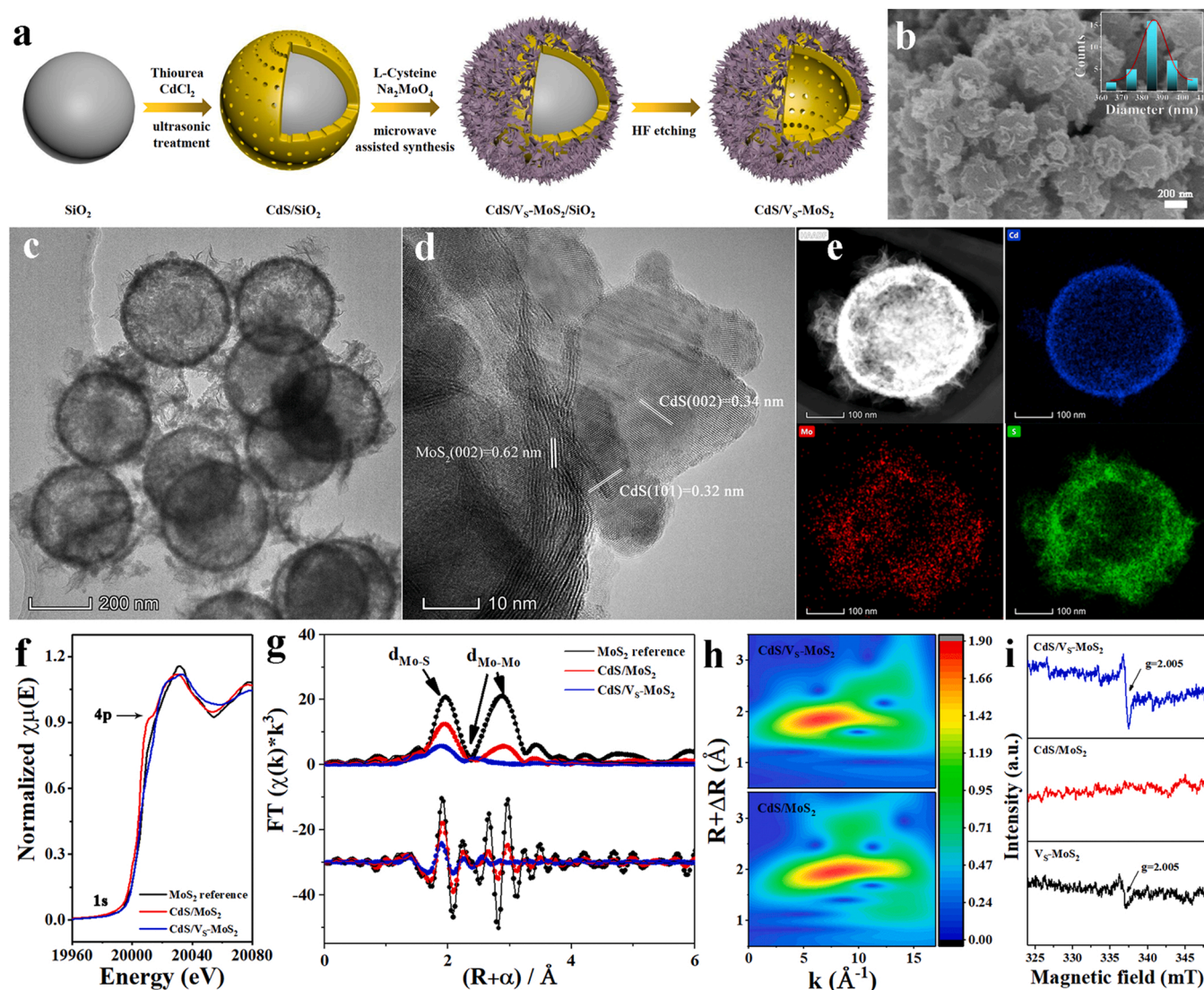The calculations of charge density difference and free energy were

Fig. 1. (a) Schematic illustration for the fabrication process of CdS/V$_S$-MoS$_2$ heterojunction; (b) SEM image, the inset shows the distribution histogram of particle size; (c) TEM image; (d) HRTEM image; (e) EDX mapping images of CdS/V$_S$-MoS$_2$-4; (f) Mo K-edge XANES spectra; (g) the corresponding FT-EXAFS spectra (point) and fitted curve (line); (h) WT-EXAFS for CdS/V$_S$-MoS$_2$ and CdS/MoS$_2$; (i) EPR spectra.

performed by the VASP package with the projector augment wave (PAW) method. And the exchange and correlation potential were simulated using the Perdew-Burke-Ernzerhof (PBE) of the generalized gradient approximation (GGA). Before calculation, the cutoff energy was set as 500 eV and a $1 \times 1 \times 1$ k-point mesh was used. Geometry optimization was terminated until the conventional energy below 10^{-6} eV and force convergence criteria below 0.02 eV/Å. The vacuum layer with the thickness of 20 Å was set to avoid the interaction between adjacent layers.

2.2.5. Operando IR spectra

Time-resolved operando IR spectra were recorded on a BRUKER-Fourier transform infrared spectrometer-TENSOR 27 (Germany) equipped with a self-installed external probe that could be directly immersed into the reaction system and monitor the changes on the photocathode. The reaction was carried out under the same conditions of PEC CO$_2$ reduction. Before testing, the electrodes were soaked in a mixed electrolyte of KHCO$_3$ and Na$_2$SO$_3$ saturated with CO$_2$ for 30 min to reach an equilibrium state. The spectrum measured without light or electricity was considered as a background spectrum. Subsequently, the time-resolved operando IR spectra were collected every 5 min during the

photoelectrocatalytic CO$_2$ reduction.

2.3. Photo and electrochemical properties of photocathodes

The cyclic voltammetry curves were measured with a three-electrode system in CO$_2$ saturated KHCO$_3$ electrolyte at different scan rates (2, 4, 6, 8, 10 mV/s). The capacitance of double-layer (Cdl) was determined by the slope of the Δj-scan rate curve. The linear sweep voltammetry (LSV) curves and transient photocurrent responses of photocathodes were carried out with a traditional two-electrode system in the electrolyte of 0.1 M KHCO$_3$ and 0.1 M Na$_2$SO$_3$ on a CHI760E electrochemical workstation equipped with a simulated solar (PLS-SXE300C) with the light density of 200 mW/cm^2. While, the electrochemical impedance spectra (EIS) and Mott–Schottky plots of photocathodes were measured on a three-electrode system under the EC condition.

The charge separation efficiency (η_{sep}) was determined based on the UV-vis spectra and LSV measured in Na$_2$SO$_3$ aqueous solution. Theoretically, the current density (J) measured on the electrochemical workstation under PEC condition is equal to the energy density of light absorption (J$_{abs}$) multiplied by the charge separation (η_{sep}) and transfer efficiency (η_{trans}), as shown in Eq. (2). The transfer efficiency (η_{trans}) can
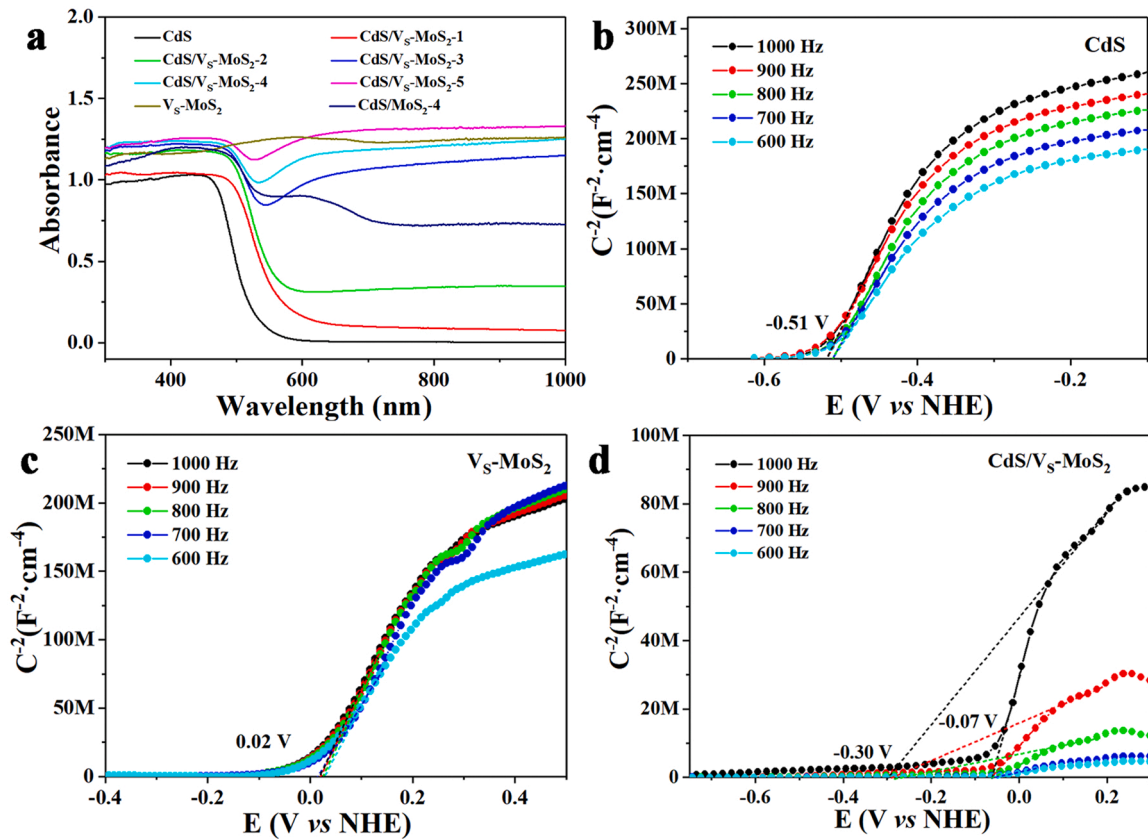
Fig. 2. (a) UV-vis absorption spectra of CdS, V_S-MoS_2, CdS/V_S-MoS_2-x and CdS/MoS_2 samples; Mott-Schottky plots of (c) CdS, (d) V_S-MoS_2 and (e) CdS/V_S-MoS_2 at different frequencies.

be regarded as 100% in the presence of Na_2SO_3. Thus, the charge separation efficiency (η_{sep}) can be calculated from Eq. (3). Meanwhile, the energy density of light absorption (J_{abs}) can be obtained by Eq. (4).

$$J = J_{abs} \times \eta_{sep} \times \eta_{trans} \qquad (2)$$

$$\eta_{sep} = J_{Na_2SO_3}/J_{abs} \qquad (3)$$

$$J_{abs} = \int_{300}^{600} \frac{LHE \times \lambda \times P_{light}}{1240} d\lambda \qquad (4)$$

LHE is the light harvesting efficiency calculated by the Eq. (5). P_{light} is the standard solar spectral irradiance at AM 1.5 G under different wavelength (nm) by National Renewable Energy Laboratory [35]. λ is the wavelength.

$$LHE = 1 - 10^{-A(\lambda)} \qquad (5)$$

A (λ) is the absorbance from UV-vis spectra.

2.4. Photoelectrocatalytic CO_2 reduction experiments

Photoelectrocatalytic CO_2 reduction was measured in a sealed quartz cell filled with 20 mL mixed solution of 0.1 M $KHCO_3$ and 0.1 M Na_2SO_3 and then bubbled with high-purity CO_2 for 30 min. The volume above the electrolyte in the sealed quartz cell is 16 mL. Subsequently, the investigation was performed in a three-electrode system of PEC cell CdS/V_S-MoS_2|SCE|$BiVO_4$ supplied by the electrochemical workstation CHI760E and irradiated by a solar simulator with light density of 200 mW/cm^2. The as-prepared photocathode, $BiVO_4$/FTO [36] and the saturated calomel electrode (SCE) were used as the working electrode, counter electrode and reference electrode, respectively. Generally, each reaction system was carried out for two hours before testing its liquid

and gas phase products.

The liquid products in electrolyte were detected and quantified by ^1H NMR spectra on a nuclear magnetic resonance spectrometer JNM-ECS400 (Japan) with H_2O peak suppression technique. A mixture solution of DMSO and D_2O (7 mmol DMSO +1 L D_2O) was used as an internal standard solution. 700 μL electrolyte and 50 μL internal standard solution were mixed for testing. The gas phase products were detected and quantified by a gas chromatograph (GC) analysis on a Varian CP-3800 GC.

The formation rate, the transfer rate of electrons (TER), selectivity of C_2 products and apparent faradaic efficiency (AFE) were calculated using the follow Eqs. (6)–(9):

$$Rate = \frac{c(DMSO) \times A(product)/A(DMSO)}{Time \times 2(cm^2)} \qquad (6)$$

$$TER = n \times Rate \qquad (7)$$

$$Selectivity \left(\% \right) = \frac{\sum_i c_i \times n_i}{\sum c \times n} \qquad (8)$$

$$AFE \left(\% \right) = \frac{\sum product\ moles \times n}{Q/96485} \qquad (9)$$

where, c(DMSO) is the concentration of DMSO (7 mmol/L); A is the area obtained from ^1H NMR spectra; n is the number of transferred electron (HCOOH=2; CH_3OH=6 CH_3CH_2OH=12; CH_2OHCH_2OH=10; H_2=2); i means C_2 product; Q (C) is the number of electrons counted on the electrochemical workstation.
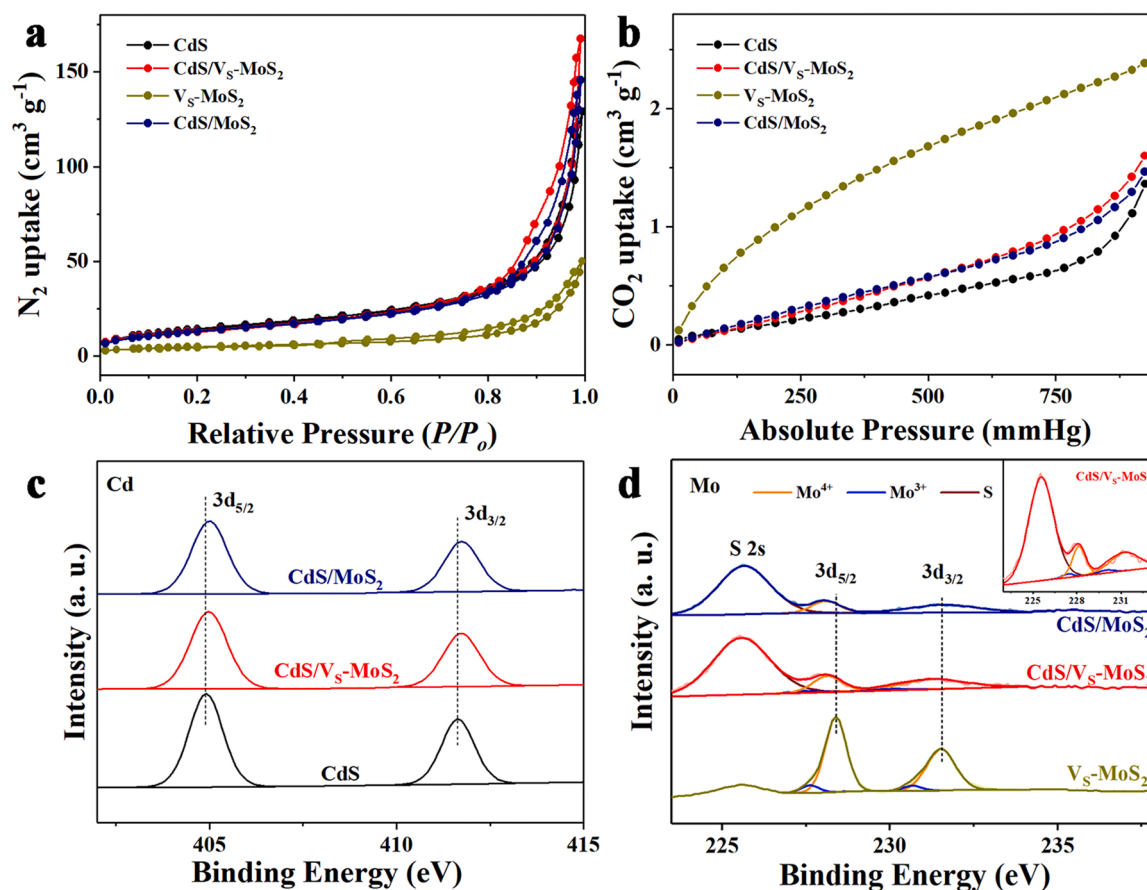
Fig. 3. (a) N_2 adsorption–desorption isotherms and (b) CO_2 adsorption isotherms of CdS, V_S-MoS_2, CdS/MoS_2 and CdS/V_S-MoS_2; High-resolution XPS spectra of (c) Cd 3d, (d) Mo 3d. The inset in (d) is a magnified XPS spectra of CdS/V_S-MoS_2.

3. Results and discussion

3.1. Physicochemical characterization

The preparation procedure of new heterojunction was given in Fig. 1a, where L-cysteine was used as sulfur source and reductive reagent to promote the formation of Mo^{3+} and in turn facilitate the existence of S-vacancies. The SEM image of CdS/V_S-MoS_2-4 (Fig. 1b) reveals the nano-spherical morphology with uniform diameter of 385 nm. The representative hollow structure can be observed in the TEM image (Fig. 1c), accompanying with the nano-crystalline CdS shell on a thickness of 12 nm. Moreover, the ultrathin V_S-MoS_2 nanosheets are located on the surfaces of CdS shell. The clear heterojunction between CdS and V_S-MoS_2 is evidenced by the overlapped lattice fringes in Fig. 1d, where the lattice spacing of 0.34 nm and 0.62 nm are assigned to the (002) planes of CdS and MoS_2, respectively [37,38]. The energy dispersive X-ray (EDX) mapping images are depicted in Fig. 1e, where the Cd element distributes in the inside shell of microsphere and the Mo element locates uniformly in the outside shell of microsphere, identifying the perfectly growth of V_S-MoS_2 on the surface of CdS hollow nanospheres. Moreover, the microstructures of SiO_2, CdS, CdS/V_S-MoS_2-x (x = 1, 2, 3, 4, 5) and V_S-MoS_2 were simultaneously investigated, as shown in Fig. S1. XRD patterns (Fig. S2) and Raman spectra (Fig. S3) of CdS/V_S-MoS_2 also demonstrate the phase and the vibration modes (characteristics in point group) of CdS and MoS_2, respectively, which confirm the successful preparation of CdS/V_S-MoS_2. For comparison, CdS/MoS_2-4 heterojunction without S-vacancies was obtained through annealing the mixture of CdS/V_S-MoS_2 and S powder under Ar gas atmosphere. The corresponding SEM and TEM images were shown in Fig. S4. It can be found that CdS/MoS_2-4 exhibits the similar

hollow nano-spherical morphology.

In order to prove the existence of S-vacancies, the X-ray absorption fine structure (XAFS) spectroscopy were measured. From the Mo K-edge X-ray absorption near edge structure (XANES) spectra in Fig. 1f, the sharp peak at 20,015 eV (confined state) and a broad band at 20,030 eV (ionized state) are related to the electron transition from 1 s to 4p orbitals of Mo^{4+}. The evidently chemical shift of CdS/V_S-MoS_2 in the summit implies the influence of S-vacancies. The Fourier transform spectra of the Mo k^3-weighted χ (k) function in R (Å) spaces of all samples were depicted in Fig. 1g. The six Mo-S single scattering paths in the first coordination sphere appears at 1.96 Å, while the peak at 2.88 Å is assigned to six Mo-Mo single scattering paths [39]. A new peak for CdS/V_S-MoS_2 is noticed at 2.43 Å, corresponding to the Mo-Mo single scattering path in the distorted Mo-S cluster. In addition, the peak intensity of CdS/V_S-MoS_2 is less and the peak width is wider than the other two catalysts. This phenomenon is caused by the smaller coordination number N and larger Debye-Waller factor σ^2 (Table S2 and Eq. (1)), indicating a more disordered structure caused by the abundant S vacancies in CdS/V_S-MoS_2. The wavelet transforms for CdS/V_S-MoS_2 is slightly shorter than CdS/MoS_2 (Fig. 1h). Furthermore, the electron spin resonance (EPR) of CdS/V_S-MoS_2, CdS/MoS_2 and V_S-MoS_2 samples were collected in Fig. 1i to further identify the presence of S vacancies. A strong signal at 337mT (Landé factor, g = 2.005) is observed for CdS/V_S-MoS_2 and V_S-MoS_2 samples, which is related to the electrons captured by S vacancies. As comparison, no EPR signal was detected for CdS/MoS_2 catalyst.

The UV-vis absorption spectra of CdS, V_S-MoS_2, CdS/V_S-MoS_2 and CdS/MoS_2 were determined and presented in Fig. 2a. The steep absorption edge of CdS is located at 550 nm and the band gap is calculated to be 2.4 eV. The V_S-MoS_2 is an indirect-bandgap semiconductor with a
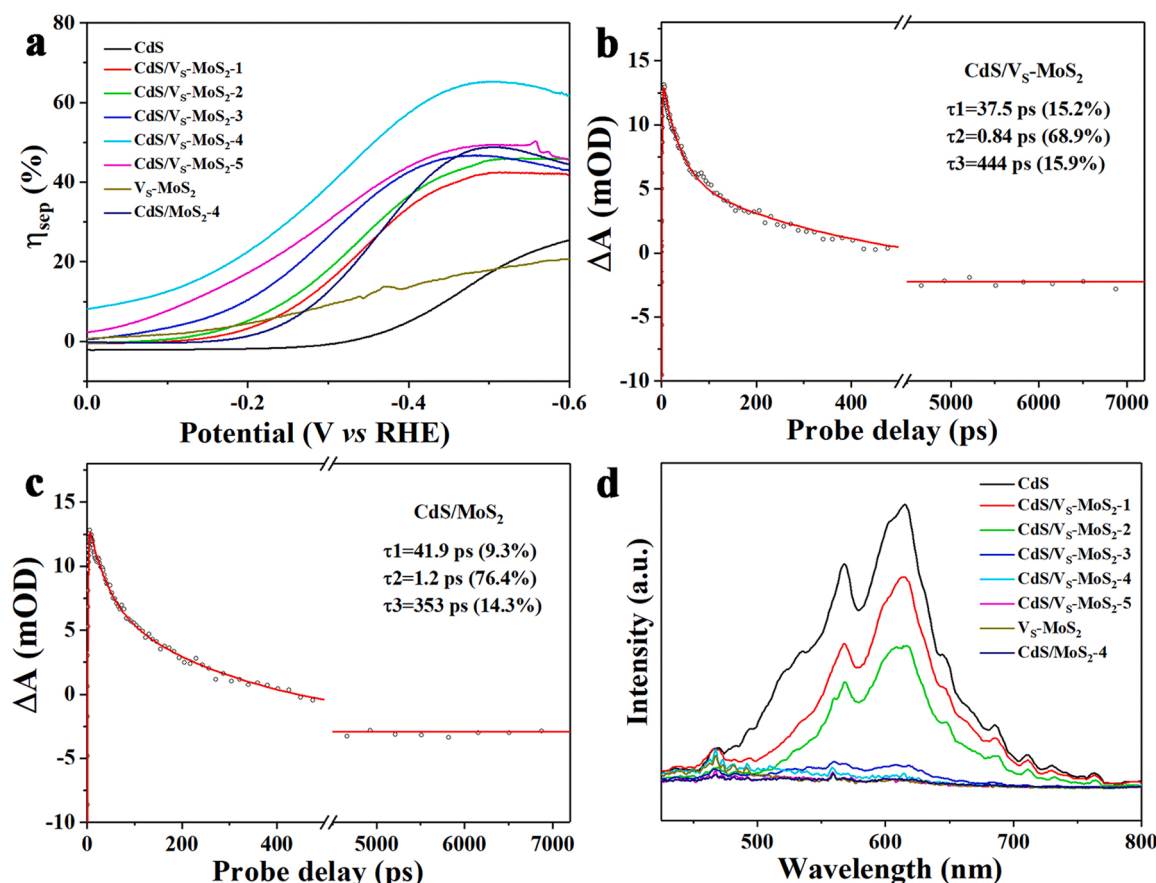
Fig. 4. (a) Charge separation efficiency of CdS, V_S-MoS_2, CdS/V_S-MoS_2-x and CdS/MoS_2; Femtosecond transient absorption (fs-TA) spectra of (b) CdS/V_S-MoS_2 and (c) CdS/MoS_2, where mOD stands for optical density; (d) PL spectra of CdS, V_S-MoS_2, CdS/V_S-MoS_2-x and CdS/MoS_2.

band gap of 1.25 eV obtained from the Tauc plots (the inset in Fig. S6). After the introduction of black V_S-MoS_2 onto the hollow CdS, the absorbance of CdS/V_S-MoS_2-x samples have increased in visible region, resulting narrower band gap than pure CdS. Besides, the positive slopes of Mott–Schottky curves in Fig. 2b-c indicate the n-type semiconductors, in which, the intercepts on the abscissa equal to the flat-band potentials (approximation to conduction band, CB) of CdS and V_S-MoS_2. When the n-n heterojunction of CdS/V_S-MoS_2 was formed (Fig. 2d), the CB values were shifted from − 0.51 V (CdS) and 0.02 V (V_S-MoS_2) to − 0.3 V and − 0.07 V, respectively. The feature of band structure for CdS/V_S-MoS_2 n-n heterojunction was depicted in Fig. S7.

The porous structures of a series of samples were characterized by N_2 adsorption–desorption isotherms (Fig. 3a). The similar IV type isotherms with H_3 type hysteretic loop ($0.5 < P/P_0 < 1$) for CdS/V_S-MoS_2 and CdS/MoS_2 exhibit numerous micropores and mesopores derived from accumulation of CdS nanocrystallites and V_S-MoS_2 nanosheets [40]. The Brunauer-Emmett-Teller surface areas (BET) of CdS, CdS/V_S-MoS_2-4, V_S-MoS_2 and CdS/MoS_2-4 samples were measured to be 52.80, 48.10, 17.32 and 48.33 m^2 g^{-1}, respectively. Obviously, the construction of the hollow structure is beneficial to the augmentation of the S_{BET}. The CO_2 adsorption capacity of samples (Fig. 3b) were in the order of V_S-MoS_2 > CdS/V_S-MoS_2-4 > CdS/MoS_2-4 > CdS. The highest CO_2 uptake value of V_S-MoS_2 would be attributed to the large numbers of S-vacancies. Although CdS/V_S-MoS_2-4 has a similar S_{BET} than CdS/MoS_2-4, it exhibits better CO_2 adsorption on account of more active sites of S-vacancies. To further explain the effect of S vacancies on CO_2 adsorption, the double layer capacitance (Cdl), proportional to electrochemical active area (ECSA), of these catalysts were tested in CO_2 saturated $KHCO_3$ electrolyte (Fig. S8). The ECSA of CdS/V_S-MoS_2-4 is 17.7 times higher than that of CdS/MoS_2-4. In addition, both the CO_2 uptake value and ECSA of

V_S-MoS_2 are much larger than that of CdS, indicating the influence of catalyst structure on CO_2 adsorption.

The X-ray photoelectron spectroscopy (XPS) was performed to identify chemical state and chemical environment of elements on the surfaces of catalysts (Fig. 3c-d). In Fig. 3c, the two peaks are ascribed to $3d_{3/2}$ and $3d_{5/2}$ levels of Cd^{2+} in all samples. Compared with CdS, the two peaks of Cd 3d in as-prepared heterojunction material have chemical shifts move to higher binding energy. Inversely, the Mo^{4+} 3d peaks of heterojunction materials shift towards lower binding energy compared with the primal V_S-MoS_2 (Fig. 3d). These oppositive shifts of Cd and Mo elements in CdS/V_S-MoS_2 are due to the transfer of electrons from CdS to V_S-MoS_2. In addition, sulfur vacancies leads to the appearance of peaks related to Mo^{3+} in XPS spectra (blue line), which can quantitatively prove the presence of sulfur vacancies. In Fig. 3d, the peak area of Mo^{3+} in CdS/V_S-MoS_2 is 8.15%, reflecting the content of sulfur vacancies is 8.15%. And the content of sulfur vacancies in V_S-MoS_2 is about 8.18%.

3.2. Photochemical and photoelectrochemical properties

The curves of linear sweep voltammetry (LSV, Fig. S9) for new catalysts give obvious increase in current density under the photoelectrocatalytic condition than electrocatalytic condition, indicating an outstanding light response. The V_S-MoS_2 sample owns the highest current density in all samples due to the excellent and intrinsic conductivity of V_S-MoS_2. The current density of heterojunction catalysts also increases with the increasing content of V_S-MoS_2.

Since the charge separation efficiency (η_{sep}) is very important to determine the CO_2 reduction ability of new heterojunctions, it was measured with the results shown in Figs. 4a and S10. The separation
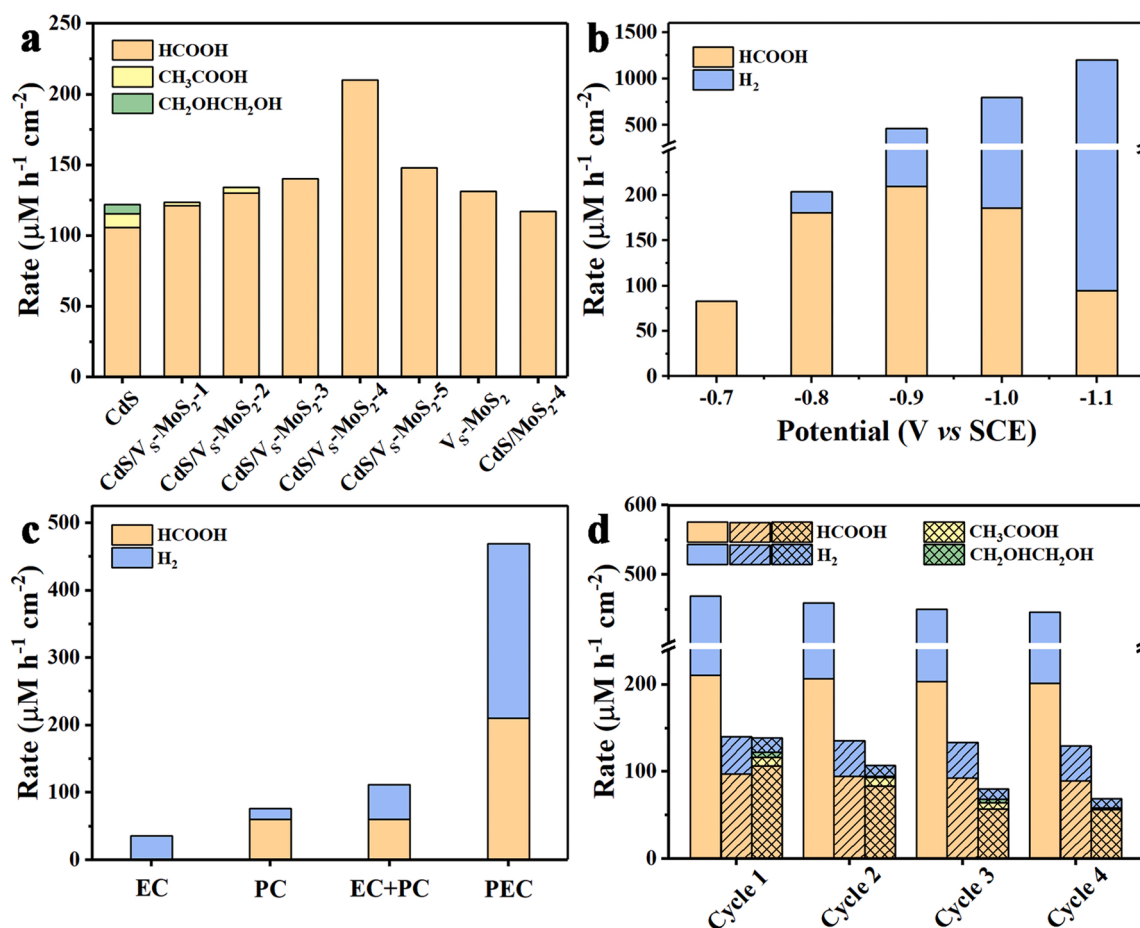
Fig. 5. (a) The formation rates of various catalysts under PEC condition at -0.9 V vs SCE; (b) The formation rates of formate for CdS/V$_S$-MoS$_2$-4 at different bias potentials; (c) Control experiments under different conditions; (d) The formation rates of CdS/V$_S$-MoS$_2$-4, CdS/MoS$_2$ (filled with slash lines) and CdS (filled with cross lines) at -0.9 V vs SCE for 4 cycles (8 h).

efficiency of CdS/V$_S$-MoS$_2$-x are higher than that of pristine CdS or V$_S$-MoS$_2$ because the heterojunctions can inhibit the recombination of photogenerated electron-hole pairs. As comparison, CdS/MoS$_2$-4 without S-vacancies has a lower charge separation efficiency than CdS/V$_S$-MoS$_2$-4 heterojunction, implying the accumulation of electrons by S-vacancies. Both the transient photocurrent responses and electrochemical impedance spectroscopy (EIS) in Figs. S11-S12 demonstrate the enhanced PEC performance of heterojunctions with S-vacancies as well.

To explore the dynamic behavior of charge transfer in depth, the femtosecond transient absorption (fs-TA) spectra were tested with 400 nm pump laser pulses (Figs. S13-S14). An absorption band feature at 468 nm in CdS/MoS$_2$ and CdS/V$_S$-MoS$_2$ can be seen and the relevant transient absorption (TA) kinetics results are presented in Fig. 4b-c. The TA kinetics curves were fitted according to the tri-exponential function fitting, in which, the decay process with τ_1 may be related to the interfacial electron transfer from CdS to V$_S$-MoS$_2$, and the fast decay process with τ_2 correspond to the trapping of electrons from CB (conduction band) of V$_S$-MoS$_2$ into the S-vacancies trap states located in the band gap, while the slowest decay process with τ_3 reflect to the recombination of electrons captured by S-vacancies and the holes in VB (valence band) [21]. This electron transfer and relaxation effect can be also understood from the scheme of energy band structure in Fig. S7. From the fitting result, τ_1, τ_2 and τ_3 are 37.5 ps (15.2%), 0.84 ps (68.9%) and 444 ps (15.9%) for CdS/V$_S$-MoS$_2$, while 41.9 ps (9.3%), 1.2 ps (76.4%) and 353 ps (14.3%) for CdS/MoS$_2$, respectively. Obviously, the CdS/V$_S$-MoS$_2$ brings about 1.3-fold increase of τ_3 than CdS/MoS$_2$, inhibiting the recombination of the relax electrons and holes. Similar

phenomenon of suppressed recombination of carriers can also be verified by the photoluminescence (PL) spectra (Fig. 4d). The emission intensities of CdS/V$_S$-MoS$_2$-x and CdS/MoS$_2$ heterojunctions decrease obviously in comparing with CdS. And the more component of V$_S$-MoS$_2$ in heterojunction materials, the less emission intensity, reflecting more photogenerated electrons to participate in the CO$_2$ reduction.

3.3. Performance of photoelectrocatalytic CO$_2$ reduction

The photoelectrocatalytic CO$_2$ reduction of the new CdS/V$_S$-MoS$_2$-x and CdS/MoS$_2$ heterojunctions were carried out by a three-electrode system in a CO$_2$-saturated electrolyte of 0.1 M KHCO$_3$ and 0.1 M Na$_2$SO$_3$ under irradiation. The major product of all catalysts is formate and the production rate is in the order of CdS/V$_S$-MoS$_2$-4 > CdS/V$_S$-MoS$_2$-5 > CdS/V$_S$-MoS$_2$-3 > CdS/V$_S$-MoS$_2$-2 > CdS/V$_S$-MoS$_2$-1 > V$_S$-MoS$_2$ > CdS/MoS$_2$ > CdS (Fig. 5a and Table S3). The optimal CdS/V$_S$-MoS$_2$-4 catalyst produce formate in a formation rate of 210 μM h^{-1} cm^{-2}, attributing to the build-in electric field at the heterojunction interface and the S-vacancies. Interestingly, no C$_2$ products was detected for CdS/V$_S$-MoS$_2$-4 catalyst, as CO$_2$ reduction occurs mainly on the external surface of the hollow structure without the supporting of confined cavity. When the potential is varied from -0.7 to -0.9 V, the formation rates of formate increase gradually (Fig. 5b and Table S4). When the bias potential is over to -0.9 V, the formation rate decreases owing to the competitive hydrogen evolution. Hence, the -0.9 V bias potential is the optimal reaction potential with the maximum formation rate of formate.

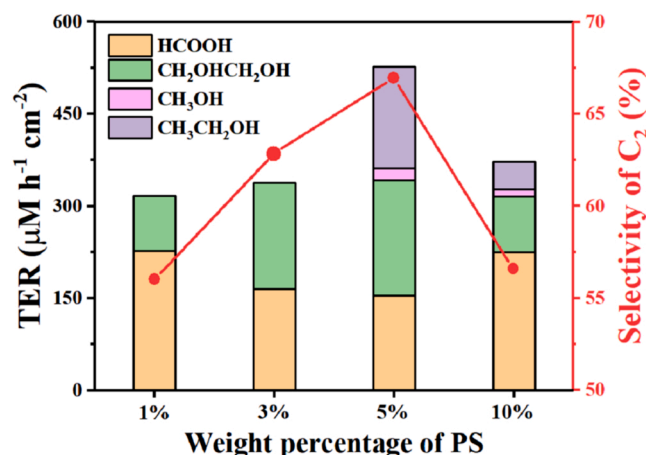Meanwhile, control experiments using the best catalyst of CdS/V$_S$-

Fig. 6. The transfer rate of electrons (TER) and selectivity of C_2 products for CdS/V_S-MoS$_2$-PS catalysts at − 0.9 V *vs.* SCE.

MoS$_2$-4 were proceeded (Fig. 5c). It can be seen that the CO_2 reduction is not happened under EC condition and only a little formate is detected under PC condition. The production rate of PEC CO_2 reduction was five times higher than the sum of the production rate under the PC and EC conditions. Subsequently, the stability of CdS/V_S-MoS$_2$-4 and CdS/MoS$_2$-4 was examined and showed a slight decrease of formation rate and current density (Figs. 5d and S18), reflecting a good stability. On the contrary, the production rate and current density of CdS dropped rapidly due to the photocorrosion of CdS itself. The SEM images and XRD patterns of the used CdS/V_S-MoS$_2$-4 catalyst after reaction have the same morphology and crystal phase of the fresh catalysts (Figs. S19 and S20). Therefore, our strategy of building heterojunctions is successful to improve the stability of catalysts.

To understand the catalytic difference between the external surface and inner surface of the hollow catalysts, a polystyrene layer without catalytic reactivity (Fig. S21) was selected to partially cover the outer surface of CdS/V_S-MoS$_2$ catalysts. When various weight percentages of polymer/catalyst were mixed and dried in vacuum, porous polystyrene-coated catalysts (named as CdS/V_S-MoS$_2$-PS) were fabricated (Fig. S22). Most of the active sites on external surface of CdS/V_S-MoS$_2$-PS catalyst would be covered and the active sites on inner surface would play a key role in CO_2 reduction. It can be seen from Fig. 6 that the selectivity of C_2 products (CH$_3$CH$_2$OH, CH$_2$OHCH$_2$OH) has been greatly improved to 67.0% with covered catalyst of CdS/V_S-MoS$_2$-PS-5%. This phenomenon confirms that the inner surface and external surface have different catalytic ability and selectivity for products. The external surfaces for hollow catalyst consisted of V_S-MoS$_2$ nanosheet tend to produce formate. While, the inner surfaces for hollow catalyst mainly consisted of CdS nanocrystals tend to generate C_2 products due to the more collision probability in the confined cavity. Comparing to the the previous reports for CdS- and MoS$_2$-based catalysts used in CO_2 reduction

(shown in Table 1), our catalysts achieved the excellent production rate with the high selectivity and apprent fradaic efficiency (AFE) of C_2 products.

The finite-element method (FEM) simulations was used to study the increased collision probability in the nano-cavity structure, leading to C_2 products. A porous circular ring with a diameter of 385 nm and a thickness of 12 nm was selected to represent the hollow catalyst. And the catalytic reaction is simplified into three steps: the diffusion of CO_2 molecules through pores on the surface of hollow sphere; the conversion of CO_2 to C_2 products and the diffusion of C_2 products through the hollow catalyst. Before reaction, CO_2 molecules are filled both inside and outside the structure (Fig. S23a, colour map). Because of the discontinuity in the diffusion of CO_2 molecules through the pores on the surface of hollow structure (Fig. S23a, arrows), the collision of CO_2 (or C_1 intermediates) inside the cavity increases, which is intuitively shown as the concentration of C_2 product inside the cavity comparing to the outside (Fig. S23b, colour map). The outflow of C_2 product by the cavity can also be found (Fig. S23b, arrows). Thus, the FEM simulations point to the regulation of morphology as a promising means to improve the selectivity of multi-carbon products in CO_2 reduction.

The isotopic labelling experiment of $^{13}CO_2$ was carried out with catalyst of CdS/V_S-MoS$_2$ to verify the carbon source in CO_2 reduction reaction. In Fig. S24a, the ^{1}H NMR signal of formate splits into two peaks at 8.08 and 8.57 ppm in terms of the coupling of proton and ^{13}C nuclei. The ^{13}C{^{1}H} NMR signals at 171.03 ppm and 124.65 ppm are assigned to the H^{13}COOH and $^{13}CO_2$, respectively (Fig. S24b). The formation of H^{13}COOH (m/z = 47) was further identified by GC-MS with an automatic headspace sampler (Fig. S25). Furthermore, the differences of external and inner surface of hollow structure in isotopic labelling experiment were revealed as following. The CdS/V_S-MoS$_2$-PS catalyst demonstrates rich isotopic products, such as ^{13}CH$_3$OH, ^{13}CH$_3$^{13}CH$_2$OH and ^{13}CH$_2$OH^{13}CH$_2$OH detected in GC-MS with an automatic headspace sampler (Fig. S26). Otherwise, small amount of isotopic product ^{13}CO could be detected by GC-MS at m/z = 29 (Fig. S27) using the catalyst of CdS/V_S-MoS$_2$-PS, which might give the evidence of carbene mechanism in the inner surface of hollow catalyst (vide infra). Herein, we must emphasize that the isotopic product ^{13}CO could not be detected by GC-MS using CdS/V_S-MoS$_2$, which verifies the different mechanisms for the formation of formic acid on the inner or external surfaces (vide infra). On this basis of above descriptions, the carbon source of products is proven to be derived from CO_2 gas.

3.4. Mechanism studies

3.4.1. The proposed mechanism and DFT calculation

To further understand the separation and transfer of electron-hole pairs, the surface charge density of catalyst CdS/V_S-MoS$_2$ were calculated by using VASP package with the projector augment wave (PAW) method. The charge density difference was depicted in Fig. 7a-b with the accumulation and depletion of electrons represented by yellow (negative charge region) and cyan (positive charge region) colors,

Table 1
Comparison with the previous CdS- and MoS$_2$-based catalysts.

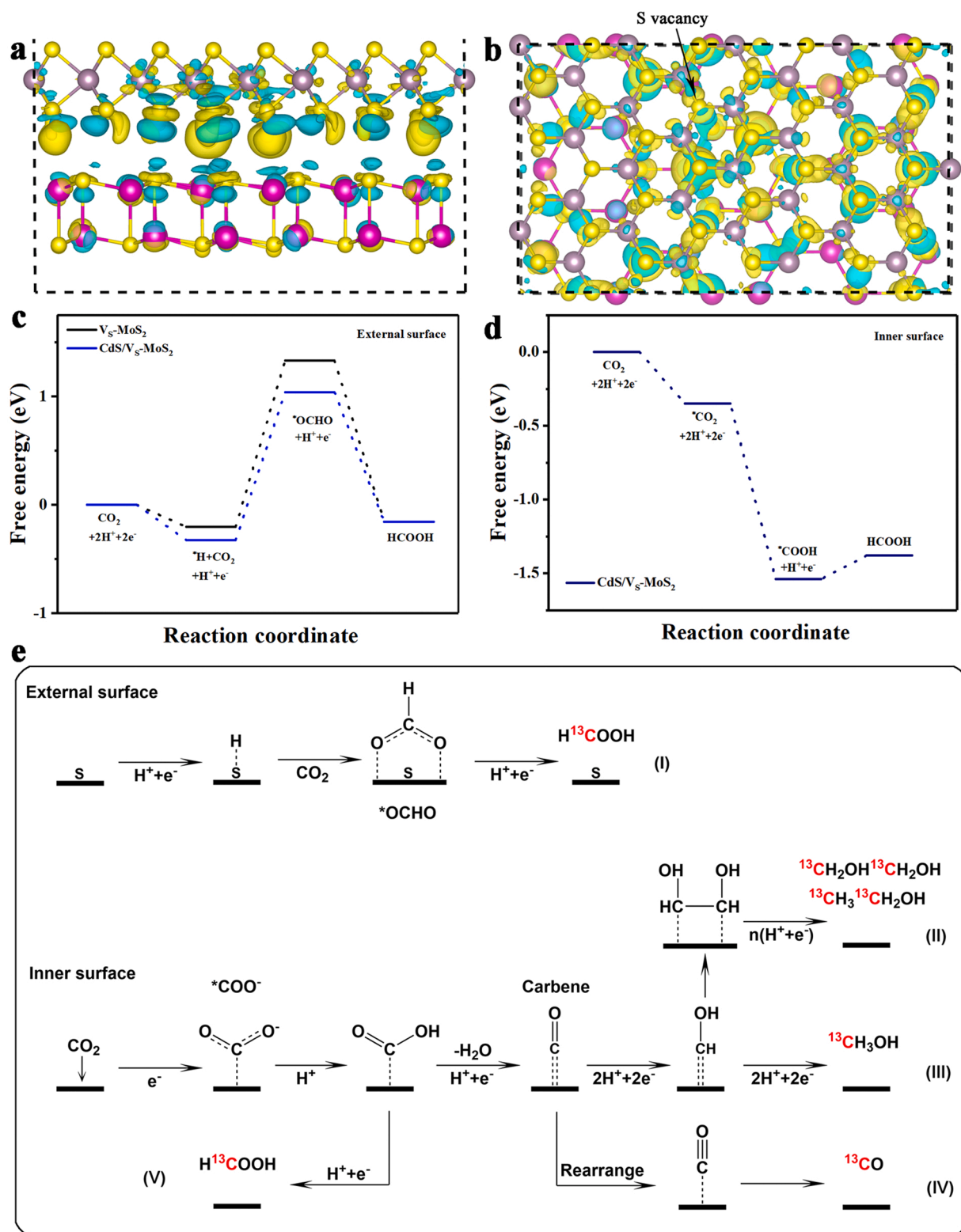| Catalyst	Main products	Rate	(Apparent) Faradaic efficiency	Selectivity of C_{2+} products	Reaction condition	Ref.
Co-CdS	CO	392 μmol h^{-1} g^{-1}	–	–	PC	[41]
MoS$_2$	CH$_3$OH CH$_3$CHO	29.6 μmol h^{-1} g^{-1}	–	11.8%	PC	[42]
BiOI/MoS$_2$/CdS	CO, CH$_4$	83.2 μmol h^{-1} g^{-1}	–	–	PC	[43]
CdS	CO, CH$_4$	389.9 μmol h^{-1} g^{-1}	–	–	PEC	[44]
CoS/MoS$_2$	CH$_3$OH, HCOOH	642.8 μM h^{-1} cm^{-2}	–	–	PEC	[45]
CdS/V_S-MoS$_2$	HCOOH	210 μM h^{-1} cm^{-2} (1680 μmol h^{-1} g^{-1})	47.2%	–	PEC	This work
CdS/V_S-MoS$_2$-PS	HCOOH, CH$_3$OH, CH$_2$OHCH$_2$OH, CH$_3$CH$_2$OH	113 μM h^{-1} cm^{-2} (904 μmol h^{-1} g^{-1})	60.3%	67.0%	PEC	This work

Fig. 7. (a) Side view and (b) top view for the calculations of charge density difference on CdS/V_S-MoS_2; Calculated free energy diagrams for CO_2 reduction to HCOOH on (c) external surface and (d) inner surface; (e) The possible reaction paths for CO_2 reduction.

respectively. The charges have been rearranged at the contact interface between CdS and V_S-MoS_2, where electrons transfer from the CdS side to the V_S-MoS_2 side. It can be seen that some yellow area is appeared in the S-vacancy (Fig. 7b) compared to the Mo-S bond without excrescent electrons.

The Gibbs free energy versus reaction coordinate via two different

pathways on the external and inner surfaces of catalyst for the formation of formic acid were carefully computerized and shown in Fig. 7c and d, respectively. On the external surface (V_S-MoS_2 (002)) of CdS/V_S-MoS_2 catalyst, one proton is easily trapped by electron in V_S site to form an active hydrogen atom (*H) with releasing the energy of 0.33 eV. When the CO_2 molecule combines with *H by carbon site to generate *OCHO
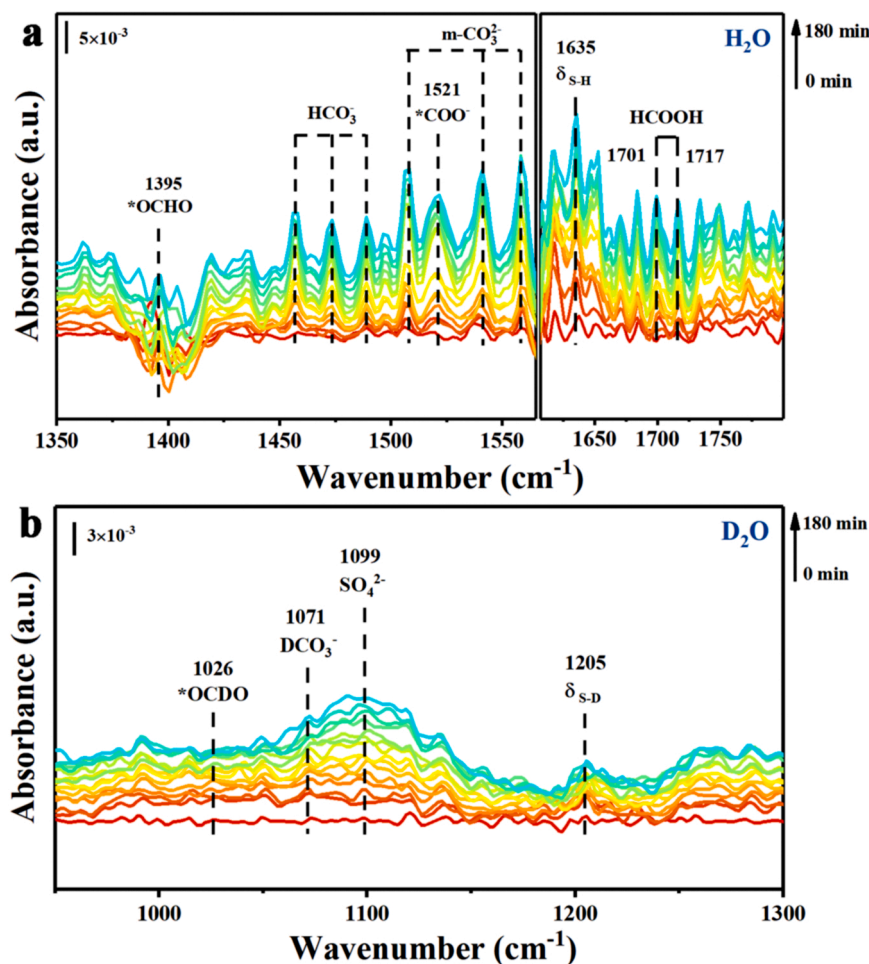
Fig. 8. Operando FT-IR spectra of the photoelectrocatalytic CO_2 reduction at -1.0 V *vs.* SCE on CdS/V_S-MoS_2 recorded in (a) H_2O solution and (b) D_2O solution.

intermediate, the activation energy on CdS/V_S-MoS_2 is about 1.36 eV less than that of V_S-MoS_2 (1.53 eV), indicating the importance of heterojunction to enhance activity of catalyst in CO_2 reduction. Interestingly, on the inner surface (CdS (002)), CO_2 is preferred to adsorb on the catalyst through the carbon site with an energy release of 0.35 eV. Next, the active hydrogen atom approaches oxygen atom of $^*CO_2$ to form $^*COOH$ intermediate which combines another $^*H$ to produce formic acid.

Based on the isotopic labelling experimental and DFT analyses, two possible reaction paths on the external and inner surfaces were proposed in Fig. 7e. On the external surface dominated by V_S-MoS_2, a $^*H$-assisted mechanism of CO_2 reduction was proposed in path I. On the inner surface, a CO_2 molecule is adsorbed on the catalyst and reduced by an electron to form $^*COO/^*CO_2^-$ intermediates. When the proton attacks the oxygen atom of $^*COO/^*CO_2^-$ specie, the $^*COOH$ intermediate is generated. When the active hydrogen atom attacks the carbon atom of $^*COOH$ specie, the formic acid could be produced via path V. If the $^*H$ attacks the hydroxy group of $^*COOH$ specie, the highly active carbene $^*=C=O$) intermediate would be generated with losing of a H_2O molecule. On the one hand, the carbene intermediate was attacked by two $^*H$ species to yield $^*CHOH$ intermediate. If two $^*CHOH$ intermediates coupled together, the C_2 products such as ethanol, glycol could be generated by path II [46]. If one $^*CHOH$ intermediate combine with two $^*H$ species, methanol would be produced via path III. On the other hand, the highly active carbene ($^*=C=O$) intermediate could rearrange to $^*CO$ with the emission of trace amount of CO through path IV. The above new paths for CO_2 reduction are in consistent with the results of isotopic labelling experiment with the GC-MS of ^{13}CO, $^{13}CH_3OH$,

$^{13}CH_3^{13}CH_2OH$ and $^{13}CH_2OH^{13}CH_2OH$ products.

3.4.2. Time-resolved operando IR spectra

The time-resolved operando IR spectra (Fig. 8) were detected to trace the reaction intermediates and understand the reaction mechanism of CO_2 reduction on CdS/V_S-MoS_2 deeply. The important intermediates proposed in DFT calculation can be observed in operando IR spectra. In Fig. 8a, an obvious peak at 1635 cm^{-1} is attributed to the bending vibration of SH (δ_{S-H}), illustrating the rationality of the first formation of active hydrogen atoms ($^*H$) at S-vacancies. A weak peak at 1395 cm^{-1} assigned to the active intermediate of $^*OCHO$ is also observed and in accordance with the literature [47], resulting formic acid by path I mechanism. In addition to reaction intermediates, the wide peak at 1521 cm^{-1} is attributed to the vibration modes of $^*COO/^*CO_2^-$ [48]. The vibration absorption peaks of formic acid and formate are located at 1701 and 1717 cm^{-1}, respectively [49]. The peaks around 1457, 1473, 1488 and 1508, 1540, 1558 cm^{-1} are assigned to the stretching vibration of HCO_3^- and CO_3^{2-}, respectively. Synchronously, the bending vibration of OH in water (δ_{O-H}) and symmetry stretching vibration of CO_2 in $CO_2 \cdot H_2O$ (Lewis acid-Lewis base adduct, ν_s) give decaying peaks at 1593 and 1401 cm^{-1} with increase of reaction time (Fig. S30), indicating the decrease of local concentration of H_2O and CO_2 and reflecting the accumulation of desired carbon-based products. To further verifying the assignment of species contained H atom, the aqueous solution was replaced by deuterium water. As prediction, the deuterium species of DS, DCO_3^-, and $^*OCDO$ were appeared at 1205, 1071 and 1026 cm^{-1} due to the low frequency with large reduced mass, respectively (Fig. 8b).

With these isotopic labelling experiments, DFT investigations and

operando IR observations in hand, we can conclude that the intermediates binding to the surfaces of catalyst by oxygen atom (*OCHO intermediates) tend to produce formic acid and the intermediates biting to surfaces by carbon atom (carbene intermediate) favor the C_2 products.

4. Conclusion

In summary, the n-n heterojunction of CdS/V_S-MoS_2 with hollow structure have been successfully fabricated. The physicochemical properties of semiconductor samples were characterized by SEM, TEM, XAFS, Mott-Schottky analysis etc. The diference between external and inner surfaces of hollow catalyst was uncovered by CdS/V_S-MoS_2-PS catalyst, which exhibited the favorable C-C coupling reaction on the inner surface. The different SH-assited mechanisms on the external and inner surfaces of hollow catalyst were discovered as well. The CO_2 molecules, intermediates and active species like *COO/*CO_2^- and *OCHO adsorbed on surface of catalyst by oxygen atom favour the formation of formate. On the contrary, those species adsorbed on surface by carbon atom are more inclined to form C_2 products. The proposed active species, intermediates and the reaction paths were proven by DFT calculations and operando IR spectra. Our results might open a new way to construct defect-rich heterojunctions with hollow nano-spherical structure for photoelectrocatalytic CO_2 reduction.

CRediT authorship contribution statement

Chunyan Liu: Conceptualization, Methodology, Investigation, Data curation, Writing – original draft, Writing – review & editing. **Yejun Xiao:** Conceptualization, Investigation. **Wenrui Wan:** Investigation. **Yan Wei:** Investigation. **Youzhi Cao:** Investigation. **Lin Hong:** Investigation. **Yingqi Wang:** Investigation. **Jiazang Chen:** Investigation. **Qiaolan Zhang:** Investigation. **Huanwang Jing:** Conceptualization, Funding acquisition, Writing – review & editing, Supervision.

Declaration of Competing Interest

The authors declare that they have no known competing financial interests or personal relationships that could have appeared to influence the work reported in this paper.

Data availability

Data will be made available on request.

Acknowledgements

Appendix A. Supporting information

Supplementary data associated with this article can be found in the online version at doi:10.1016/j.apcatb.2023.122394.

References

[1] Halmann, Photoelectrochemical reduction of aqueous carbon dioxide on p-type gallium phosphide in liquid junction solar cells, Nature 275 (1978) 115–116.

[2] X.X. Chang, T. Wang, P.P. Yang, G. Zhang, J.L. Gong, The development of cocatalysts for photoelectrochemical CO_2 reduction, Adv. Mater. 31 (2019) 1804710.

[3] J.Y. Wang, Y.J. Guan, X.G. Yu, Y.Z. Cao, J.Z. Chen, Y.L. Wang, B. Hu, H.W. Jing, Photoelectrocatalytic reduction of CO_2 to paraffin using p-n heterojunctions, Iscience 23 (2020), 100768.

[4] J. Xiong, P. Song, J. Di, H.M. Li, Ultrathin structured photocatalysts: A versatile platform for CO_2 reduction, Appl. Catal. B-Environ. 256 (2019) 1734–1737.

[5] Y.X. Pan, Y. You, S. Xin, Y.T. Li, G.T. Fu, Z.M. Cui, Y.L. Men, F.F. Cao, S.H. Yu, J. B. Goodenough, Photocatalytic CO_2 reduction by carbon coated Indium-oxide nanobelts, J. Am. Chem. Soc. 139 (2017) 4123–4129.

[6] X.F. Cui, J. Wang, B. Liu, S. Ling, R. Long, Y.J. Xiong, Turning Au nanoclusters catalytically active for visible-light-driven CO_2 reduction through bridging ligands, J. Am. Chem. Soc. 140 (2018) 16514–16520.

[7] S. Zhang, P. Kang, T.J. Meyer, Nanostructured tin catalysts for selective electrochemical reduction of crbon dioxide to formate, J. Am. Chem. Soc. 136 (2014) 1734–1737.

[8] C.M. Ding, C.C. Feng, Y.H. Mei, F.Y. Liu, H. Wang, M. Dupuis, C. Li, Carbon nitride embedded with transition metals for selective electrocatalytic CO_2 reduction, Appl. Catal. B-Environ. 268 (2020), 118391.

[9] B. Chang, X.G. Zhang, Z.J. Min, W.W. Lu, Z.Y. Li, J.K. Qiu, H.Y. Wang, J. Fan, J. J. Wang, Efficient electrocatalytic conversion of CO_2 to syngas for the Fischer-Tropsch process using a partially reduced Cu_3P nanowire, J. Mater. Chem. A 9 (2021) 17876–17884.

[10] Q. Shen, J. Ma, X.F. Huang, N.J. Yang, G.H. Zhao, Enhanced carbon dioxide conversion to formate on a multi-functional synergistic photoelectrocatalytic interface, Appl. Catal. B-Environ. 219 (2017) 45–52.

[11] J. Cheng, M. Zhang, J.Z. Liu, J.H. Zhou, K.F. Cen, A. Cu, foam cathode used as a Pt-RGO catalyst matrix to improve CO_2 reduction in a photoelectrocatalytic cell with a TiO_2 photoanode, J. Mater. Chem. A 3 (2015) 12947–12957.

[12] B. Shan, S. Vanka, T.T. Li, L. Troian-Gautier, M.K. Brennaman, Z.T. Mi, T.J. Meyer, Binary molecular-semiconductor p-n junctions for photoelectrocatalytic CO_2 reduction, Nat. Energy 4 (2019) 290–299.

[13] J.J. Wang, S. Lin, N. Tian, T.Y. Ma, Y.H. Zhang, H.W. Huang, Nanostructured metal sulfides: Classification, modification strategy, and solar-driven CO_2 reduction application, Adv. Funct. Mater. 31 (2021) 2008008.

[14] Z.R. Tang, B. Han, C. Han, Y.J. Xu, One dimensional CdS based materials for artificial photoredox reactions, J. Mater. Chem. A 5 (2017) 2387–2410.

[15] D. Li, K.X. Yang, J.H. Lian, J.Q. Yan, S.Z. Liu, Powering the world with solar fuels from photoelectrochemical CO_2 reduction: basic principles and recent advances, Adv. Energy Mater. 12 (2022) 2201070.

[16] Q.L. Wang, X.K. Wang, Z.H. Yu, X.X. Jiang, J.J. Chen, L.M. Tao, M.K. Wang, Y. Shen, Artificial photosynthesis of ethanol using type-II $g-C_3N_4/ZnTe$ heterojunction in photoelectrochemical CO_2 reduction system, Nano Energy 60 (2019) 827–835.

[17] S.J. Xia, Y. Meng, X.B. Zhou, J.L. Xue, G.X. Pan, Z.M. Ni, $Ti/ZnO-Fe_2O_3$ composite: Synthesis, characterization and application as a highly efficient photoelectrocatalyst for methanol from CO_2 reduction, Appl. Catal. B-Environ. 187 (2016) 122–133.

[18] J.W. Li, J.R. Feng, X.M. Guo, H.L. Fang, J.Y. Chen, C.R. Ma, R.C. Li, Y.Y. Wang, Z. B. Rui, Defect-band bridge photothermally activates Type III heterojunction for CO_2 reduction and typical VOCs oxidation, Appl. Catal. B-Environ. 309 (2022), 121248.

[19] Y. Xu, F. Wang, S. Lei, Y. Wei, D. Zhao, Y. Gao, X. Ma, S. Li, S. Chang, M. Wang, H. Jing, In situ grown two-dimensional TiO_2/Ti_3CN MXene heterojunction rich in Ti^{3+} species for highly efficient photoelectrocatalytic CO_2 reduction, Chem. Eng. J. (2022), 139392.

[20] R. Das, S. Sarkar, R. Kumar, S.D. Ramarao, A. Cherevotan, M. Jasil, C.P. Vinod, A. K. Singh, S.C. Peter, Noble-metal-free heterojunction photocatalyst for selective CO_2 reduction to methane upon induced strain relaxation, ACS Catal. 12 (2022) 687–697.

[21] X.C. Jiao, Z.W. Chen, X.D. Li, Y.F. Sun, S. Gao, W.S. Yan, C.M. Wang, Q. Zhang, Y. Lin, Y. Luo, Y. Xie, Defect-mediated electron-hole separation in one-unit-cell $ZnIn_2S_4$ layers for boosted solar-driven CO_2 reduction, J. Am. Chem. Soc. 139 (2017) 7586–7594.

[22] S. Gao, Z.T. Sun, W. Liu, X.C. Jiao, X.L. Zu, Q.T. Hu, Y.F. Sun, T. Yao, W.H. Zhang, S.Q. Wei, Y. Xie, Atomic layer confined vacancies for atomic-level insights into carbon dioxide electroreduction, Nat. Commun. 8 (2017) 14503.

[23] J.Y. Liu, X.Q. Gong, R.X. Li, H.T. Shi, S.B. Cronin, A.N. Alexandrova, Photo) Electrocatalytic CO_2 reduction at the defective anatase TiO_2 (101) surface, ACS Catal. 10 (2020) 4048–4058.

[24] H. Han, S. Jin, S. Park, Y. Kim, D. Jang, M.H. Seo, W.B. Kim, Plasma-induced oxygen vacancies in amorphous MnO_x boost catalytic performance for electrochemical CO_2 reduction, Nano Energy 79 (2021) 105492.

[25] C.B. Bie, B.C. Zhu, F.Y. Xu, L.Y. Zhang, J.G. Yu, In situ grown monolayer N-doped graphene on CdS hollow spheres with seamless contact for photocatalytic CO_2 reduction, Adv. Mater. 31 (2019) 1902868.

[26] P. Zhang, S.B. Wang, B.Y. Guan, X.W. Lou, Fabrication of CdS hierarchical multi-cavity hollow particles for efficient visible light CO_2 reduction, Energ. Environ. Sci. 12 (2019) 164–168.

[27] L. Zou, R.J. Sa, H. Zhong, H.W. Lv, X.C. Wang, R.H. Wang, Photoelectron transfer mediated by the interfacial electron effects for boosting visible-light-driven CO_2 reduction, ACS Catal. 12 (2022) 3550–3557.

[28] M. Zhou, S.B. Wang, P.J. Yang, C.J. Huang, X.C. Wang, Boron carbon nitride semiconductors decorated with CdS nanoparticles for photocatalytic reduction of CO_2, ACS Catal. 8 (2018) 4928–4936.

[29] W.L. Dai, J.J. Yu, Y.Q. Deng, X. Hu, T.Y. Wang, X.B. Luo, Facile synthesis of MoS_2/Bi_2WO_6 nanocomposites for enhanced CO_2 photoreduction activity under visible light irradiation, Appl. Surf. Sci. 403 (2017) 230–239.

[30] W. Zheng, W. Feng, X. Zhang, X.S. Chen, G.B. Liu, Y.F. Qiu, T. Hasan, P.H. Tan, P. A. Hu, Anisotropic growth of nonlayered CdS on MoS_2 monolayer for functional vertical heterostructures, Adv. Funct. Mater. 26 (2016) 2648–2654.

[31] W. Stöber, E.B.A. Fink, Controlled growth of monodisperse silica spheres in the micron size range, J. Colloid Interface Sci. 26 (1968) 62.

[32] A.A. Unver, D.M. Himmelblau, Diffusion coefficients of CO_2, C_2H_4, C_3H_6 and C_4H_8 in water from 6° to 65° C, J. Chem. Eng. Data 9 (1964) 428–431.

[33] L. Hao, D.G. Leist, Binary mutual diffusion coefficients of aqueous alcohols. Methanol to 1-heptanol, J. Chem. Eng. Data 41 (1996) 210–213.

[34] T.T. Zhuang, Y.J. Pang, Z.Q. Liang, Z.Y. Wang, Y. Li, C.S. Tan, J. Li, C.T. Dinh, P. De Luna, P.L. Hsieh, T. Burdyny, H.H. Li, M.X. Liu, Y.H. Wang, F.W. Li, A. Proppe, A. Johnston, D.H. Nam, Z.Y. Wu, Y.R. Zheng, A.H. Ip, H.R. Tan, L.J. Chen, S.H. Yu, S.O. Kelley, D. Sinton, E.H. Sargent, Copper nanocavities confine intermediates for efficient electrosynthesis of C3 alcohol fuels from carbon monoxide, Nat. Catal. 1 (2018) 946–951.

[35] F. Li, J. Li, J. Zhang, L.L. Gao, X.F. Long, Y.P. Hu, S.W. Li, J. Jin, J.T. Ma, NiO nanoparticles anchored on phosphorus-doped-Fe_2O_3 nanoarrays: An efficient hole extraction p-n heterojunction photoanode for water oxidation, Chemsuschem 11 (2018) 2156–2164.

[36] T.W. Kim, K.S. Choi, Nanoporous $BiVO_4$ photoanodes with dual-layer oxygen evolution catalysts for solar water splitting, Science 343 (2014) 990–994.

[37] F.Y. Gao, S.J. Hu, X.L. Zhang, Y.R. Zheng, H.J. Wang, Z.Z. Niu, P.P. Yang, R.C. Bao, T. Ma, Z. Dang, Y. Guan, X.S. Zheng, X. Zheng, J.F. Zhu, M.R. Gao, S.H. Yu, High-curvature transition-metal chalcogenide nanostructures with a pronounced proximity effect enable fast and selective CO_2 electroreduction, Angew. Chem. Int. Ed. 59 (2020) 8706–8712.

[38] Z.F. Zhang, X.Z. Song, S.H. Liu, F.F. Sun, G.C. Liu, Z.Q. Tan, Template-assisted synthesized MoS_2/polyaniline hollow microsphere electrode for high performance supercapacitors, Electrochim. Acta 312 (2019) 1–10.

[39] F. Cesano, S. Bertarione, A. Piovano, G. Agostini, M.M. Rahman, E. Groppo, F. Bonino, D. Scarano, C. Lamberti, S. Bordiga, L. Montanari, L. Bonoldi, R. Millini, A. Zecchina, Model oxide supported MoS_2 HDS catalysts: structure and surface properties, Catal. Sci. Technol. 1 (2011) 123–136.

[40] S.P. Ding, X.F. Liu, Y.Q. Shi, Y. Liu, T.F. Zhou, Z.P. Guo, J.C. Hu, Generalized synthesis of ternary sulfide hollow structures with enhanced photocatalytic performance for degradation and hydrogen evolution, ACS Appl. Mater. Inter. 10 (2018) 17911–17922.

[41] G.X. Zhao, W. Zhou, Y.B. Sun, X.K. Wang, H.M. Liu, X.G. Meng, K. Chang, J.H. Ye, Efficient photocatalytic CO_2 reduction over Co(II) species modified CdS in aqueous solution, Appl. Catal. B-Environ. 226 (2018) 252–257.

[42] R.A. Geioushy, S.M. El-Sheikh, I.M. Hegazy, A. Shawky, S. El-Sherbiny, A.H. T. Kandil, Insights into two-dimensional MoS_2 sheets for enhanced CO_2 photoreduction to C-1 and C-2 hydrocarbon products, Mater. Res. Bull. 118 (2019) 110499.

[43] Y. Li, H.H. Luo, Y.F. Bao, S.Y. Guo, D.Y. Lei, Y. Chen, Construction of hierarchical $BiOI/MoS_2/CdS$ heterostructured microspheres for boosting photocatalytic CO_2 reduction under visible light, Sol. RRL 5 (2021) 2100051.

[44] Z.P. Li, H.B. Cheng, Y.F. Li, W. Zhang, Y. Yu, H_2O_2 treated CdS with enhanced activity and improved stability by a weak negative bias for CO_2 photoelectrocatalytic reduction, ACS Sustain. Chem. Eng. 7 (2019) 4325–4334.

[45] H. Peng, J. Lu, C.X. Wu, Z.X. Yang, H. Chen, W.J. Song, P.Q. Li, H.Z. Yin, Co-doped MoS_2 NPs with matched energy band and low overpotential high efficiently convert CO_2 to methanol, Appl. Surf. Sci. 353 (2015) 1003–1012.

[46] J.Y. Wang, J.P. Ma, Q.L. Zhang, Y. Chen, L. Hong, B. Wang, J.Z. Chen, H.W. Jing, New heterojunctions of CN/TiO_2 with different band structure as highly efficient catalysts for artificial photosynthesis, Appl. Catal. B-Environ. 285 (2021) 119781.

[47] Y.Y. Cheng, J. Hou, P. Kang, Integrated capture and electroreduction of flue gas CO_2 to formate using amine functionalized SnO_x nanoparticles, ACS Energy Lett. 6 (2021) 3352–3358.

[48] Z.F. Jiang, H.L. Sun, T.Q. Wang, B. Wang, W. Wei, H.M. Li, S.Q. Yuan, T.C. An, H. J. Zhao, J.G. Yu, P.K. Wong, Nature-based catalyst for visible-light-driven photocatalytic CO_2 reduction, Energ. Environ. Sci. 11 (2018) 2382–2389.

[49] J. Li, Y.H. Ye, L.Q. Ye, F.Y. Su, Z.Y. Ma, J.D. Huang, H.Q. Xie, D.E. Doronkin, A. Zimina, J.D. Grunwaldt, Y. Zhou, Sunlight induced photo-thermal synergistic catalytic CO_2 conversion via localized surface plasmon resonance of $MoO_{3−x}$, J. Mater. Chem. A 7 (2019) 2821–2830.